UNIVERSITÉ DE GENÈVE

Archive ouverte UNIGE
https://archive-ouverte.unige.ch

Article scientifique | Article | 2017

Accepted version | Open Access

This is an author manuscript post-peer-reviewing (accepted version) of the original publication. The layout of the published version may differ .

[4]Helicene-Squalene Fluorescent Nanoassemblies for Specific Targeting of Mitochondria in Live-Cell Imaging

Babic, Andréj; Pascal, Simon; Duwald, Romain; Moreau, Dimitri; Lacour, Jérôme; Allémann, Eric

How to cite

BABIC, Andréj et al. [4]Helicene-Squalene Fluorescent Nanoassemblies for Specific Targeting of Mitochondria in Live-Cell Imaging. In: Advanced Functional Materials, 2017, vol. 27, n° 33, p. 1701839. doi: 10.1002/adfm.201701839

This publication URL: https://archive-ouverte.unige.ch/unige:96561
Publication DOI: 10.1002/adfm.201701839

© This document is protected by copyright. Please refer to copyright holder(s) for terms of use.

[4]Helicene-squalene fluorescent nanoassemblies for specific targeting of mitochondria in live-cell imaging

Andrej Babič,[a,*] Simon Pascal,[b] Romain Duwald,[b] Dimitri Moreau,[c]

Jérôme Lacour,[b,*] and Eric Allémann[a,*]

[a] Pharmaceutical Technology, School of Pharmaceutical Sciences, University of Geneva, University of Lausanne, Rue Michel Servet 1, 1211 Geneva, Switzerland.

[b] Department of Organic Chemistry, University of Geneva, Quai Ernest Ansermet 30, CH-1211 Geneva 4, Switzerland.

[c] Department of Biochemistry, University of Geneva, Quai Ernest Ansermet 30, CH-1211 Geneva 4, Switzerland.

KEYWORDS Nanoassemblies, squalene, fluorescence, cationic helicenes, red to near-IR imaging, mitochondria

ABSTRACT Ester, amide and directly-linked composites of squalene and cationic diaza [4]helicenes **1** were readily prepared. These lipid-dye constructs **2**, **3** and **4** gave in aqueous media monodispersed spherical nanoassemblies around 100-130 nm in diameter with excellent stability for several months. Racemic and enantiopure nanoassemblies of compound **2** were fully characterized, including by TEM and cryo-TEM imaging that did not reveal higher order supramolecular structures. Investigations of their (chir)optical properties showed red absorption maxima *ca.* 600 nm and red fluorescence spanning up to the near-infrared region, with average Stokes shifts of 1350-1550 cm^{-1}. Live-cell imaging by confocal microscopy revealed rapid internalization on the minute time scale and organelle-specific accumulation. Co-localization with MitoTracker in several cancer cell lines demonstrated a specific staining of mitochondria by the [4]helicene-squalene nanoassemblies. To our knowledge, it is the first report of a sub-cellular targeting by squalene-based nanoassemblies.

INTRODUCTION

Self-assembled nanoparticles constitute an emerging domain in nanotechnology.[1] In this context, squalene based nanoassemblies (NAs) have arisen as a robust platform in theranostic nanomedicine.[2] Squalene is a natural triterpene and biosynthetic precursor of steroids. It has been extensively used as an excipient for the preparation of lipid emulsions, in particular for the delivery of vaccines, various active pharmaceutical ingredients and genes.[3] Furthermore, by attaching covalently a squalene chain to a drug, in a so-called "squalenoylation" protocol, improved pharmacokinetics of hydrophilic cytostatics and improved therapeutic outcomes are observed, in particular in cancer chemotherapy.[4] Squalenoylation has also been found to enhance drug stability, lower toxicity, improve bioavailability and mean residence time of drugs in the systemic circulation.[5] This is perhaps best demonstrated by gemcitabine-squalene conjugate (Chart 1) which shows superior anti-cancer efficacy and better tolerability *in vivo*.[6] Further advantages of squalene-based self-assembled nano systems are simplicity of synthesis and reproducibility of nanoparticle formation. Very importantly, besides improving therapeutic indexes of hydrophilic drugs, the attachment of squalene moieties also allows water "solubilization" of poorly water-soluble molecules by inverted water in oil system, thus allowing biomedical applications of these compounds.

In another context, fluorescent nanoparticles have found applications in many fields ranging from biosensors[7] to bioimaging[8] and theranostics.[9] They provide robust, reproducible and simple nano-platforms with unique optical properties coming from their relatively simple building blocks. New far-red and near-infrared (NIR) nanoparticle dyes are highly sought in biomedicine since they allow better imaging resolution due to their absorption and fluorescence properties located in the transparency window of biological tissues around 650-1300 nm.[10] So far, helicenes – that are

ortho-condensed polycyclic aromatic compounds – are rarely used in bioimaging,[11] even though their helical geometry (configuration) may be useful for selective DNA binding.[12] In fact, their (high energy) fluorescence in the blue-green spectral range of visible light limits biological applications. In addition, as classical helicenes are extended polyaromatics, aggregation occurs in aqueous media, limiting thus solubility and modifying optical characteristics. However, aggregative properties can become assets, as demonstrated by Latterini and co-workers who observed emission at longer wavelengths due to aggregation of the *N*-methyl-aza-[5]helicenium dye in cytoplasm (Chart 1).[12f] More recently, Lu, Wang, Chen *et al.* took advantage of the low water solubility of racemic tetrahydro[5]helicene derivatives to prepare self-assemblies by re-precipitation techniques (Chart 1).[13] The nanoparticles displayed bright visible colorations, efficient staining of HeLa cells and low cytotoxicity. While these examples proved that helicenes can be used as efficient fluorophores in bioimaging applications, the poor configurational stability or racemic nature of the [5]helicene derivatives did not allow an insight on the influence of stereochemistry on the aggregation / nanoparticle self-assembly or on the chiroptical properties of the dyes.

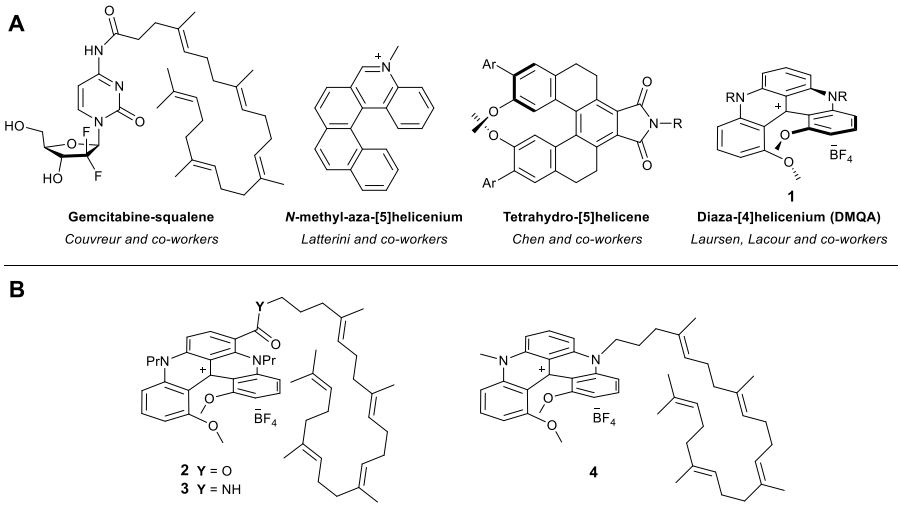

Chart 1. Reported structures of gemcitabine-squalene conjugate and of [5] and [4]helicenes used for bioimaging (A); Diaza [4]helicene-squalene composites **2**, **3**, and **4** under the scope of this study (B).

In this context, helical dimethoxyquinacridium cations **1** (DMQA, Chart 1)[14] appeared as choice candidates for bioimaging applications since these cationic [4]helicenes possess high configurational and chemical stabilities, coupled with strong orange-red emission.[15] Moreover, DMQA derivatives can be synthesized as racemates in only two steps and straightforward resolution protocols permit the isolation of the left- and right-handed enantiomers, respectively of *M* and *P* configurations, in gram scale.[16] Finally, by late stage functionalization and derivatizations, the tuning of solubility and of (chiro)optical properties is readily feasible,[17] making these versatile [4]helicenes suitable building blocks for supramolecular nanoconstructs.

Herein, the synthesis of [4]helicene-squalene constructs **2**, **3** and **4** is presented using a composition of functionalized diaza [4]helicenes and squalene chains as nanoassembly scaffold. The new red-emitting conjugates were comprehensively characterized in racemic and enantiopure forms for their (chir)optical properties as single molecules and as nanoconstructs. The nano-helicene supramolecular composites were tested on several cancer cell lines and demonstrated unique staining properties of mitochondria. To our knowledge, it is the first report of a squalene based nanoassembly system which displays selective subcellular accumulation in cancer cells.

RESULTS AND DISCUSSION

Synthesis

Preparations of [4]helicene cations **2**, **3** and **4** from tris(2,6-dimethoxyphenyl)methylium tetrafluoroborate salt **5** are depicted in Scheme 1.. Briefly, the synthesis of DMQA cations is classically achieved by *N*-cyclizations of carbenium precursor **5** in presence of bridging nucleophiles such as aliphatic amines (typically *n*-propylamine).[14, 18] Furthermore, DMQA

derivatives can be post-functionalized by reactions with electrophilic reagents, such as Eschenmoser's $CH_2=N^+Me_2$ iminium ion.[17a] The resulting aldehyde adduct can be oxidized to a carboxylate functional group under Pinnick-Kraus conditions, affording zwitterionic diaza [4]helicene **6** (Scheme 1, A), which is a useful synthetic intermediate to access highly fluorescent dyes *via* esterification and amidation reactions.[17]

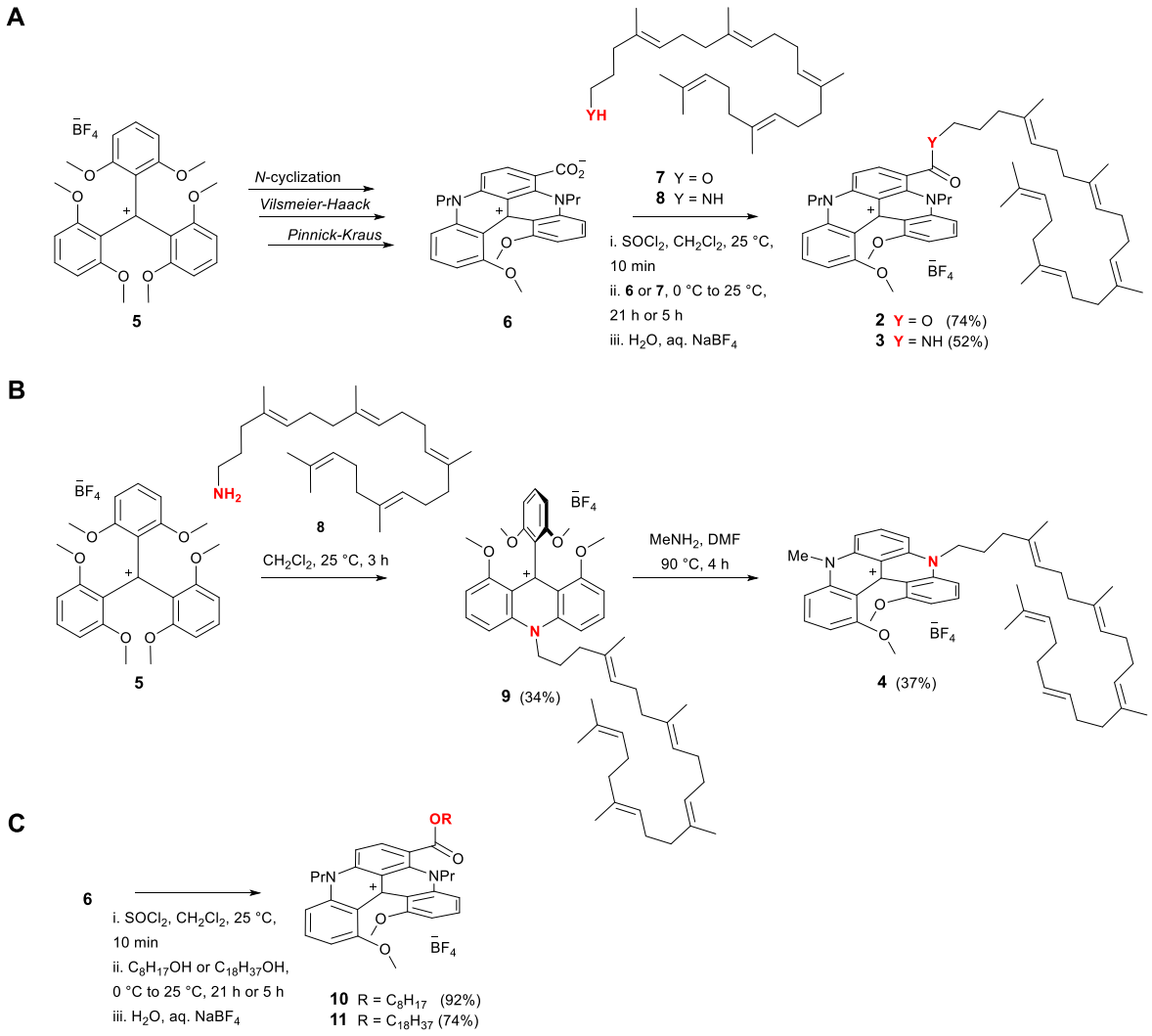

Scheme 1. Synthetic routes to diaza [4]helicene-squalene composites. Starting from carbenium precursor **5** conjugation of squalene can be achieved through coupling of functionalized DMQA to squalene amine or alcohol (A) or integrated into the [4]helicene core by reacting carbenium precursor **5** with squalene amine **8** then closing the system with methylamine, affording construct **4** (B). Reference compounds **10** and **11** directly prepared from **6** by esterification (C).

In fact, carboxylate **6** was converted to the corresponding acyl chloride with $SOCl_2$ and subjected to (slow) nucleophilic substitution reactions at 20 °C in presence of an excess of squalene alcohol **7** or amine **8** derivatives; these latter molecules being obtained from squalene using four and five step synthetic procedures, respectively.[19] The corresponding ester and amide-functionalized [4]helicenes **2** and **3** were isolated after purification by flash column chromatography in 74% and 52% yield, respectively.

In a different approach (Scheme 1, B), it was possible to synthesize non-symmetrical diaza [4]helicene **4**. First, acridinium-squalene intermediate **9** (34%) was prepared selectively by treatment at 20 °C of carbenium **5** with squalene amine **8**. Then, at 90 °C, addition of an excess of methylamine (aqueous solution) afforded squalene-containing diaza [4]helicene **4** in 37% yield.

Compounds **2**, **3** and **4** were synthesized as racemates and fully characterized by ^{1}H, ^{13}C and ^{19}F NMR, UV-vis, IR spectroscopies, and high-resolution mass spectrometry. In the case of **2**, starting from either *M* or *P* building block **6**,[17b] it was possible to reproduce the synthesis in enantiopure series and hence investigate the physico-chemical properties of NAs made of *rac*-**2**, *M*-**2** or *P*-**2** respectively (Figure 1). Compared to racemic mixtures the enantiopure helicenes are known to interact differently with biological targets[20] and display dissimilar aggregation properties[21] which are highly relevant in the context of self-assembled materials.

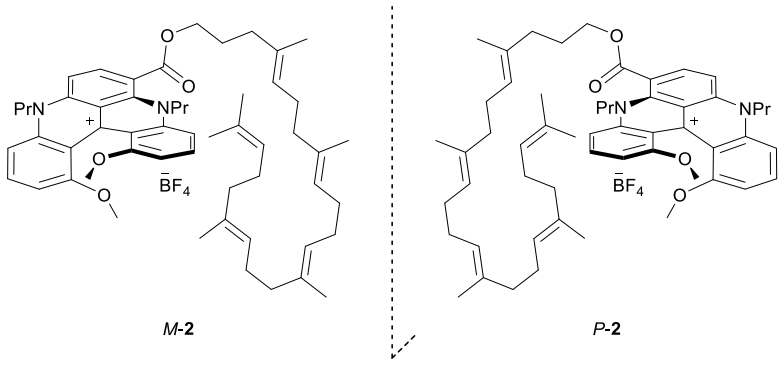

Figure 1. *M* (left) and *P* (right) enantiomers of **2**.

Finally, reference compounds **10** and **11** (Scheme 1, C), containing linear aliphatic C_8 and C_{18} chains on the ester group, were synthesized using an approach similar to that of **2**. These relatively simple conjugates, synthesized in 92% and 74% yield respectively (see Supplementary information), will serve as controls in nanoassembly experiments.

Preparation and physico-chemical characterization of racemic and enantiopure nanoassemblies

The NAs were obtained by a controlled nanoprecipitation in ultrapure water from a mixture of acetone and ethanol (Figure S18). The organic to aqueous phase volume ratios, the rate of addition and rate of evaporation were all rigorously controlled to give maximum robustness and repeatability to the nanoassembly process. All of the squalene-helicenes constructs could be effectively formulated into nanosystems. The NAs were first analyzed by dynamic light scattering (DLS). In general the quasi-elastic light scattering showed monodisperse NAs around 100 nm with low to very low polydispersity indexes (PDI). Figure 2 presents the size distribution of **nano-*rac*-2** (nanoassembly constructed from ***rac*-2**). The PDI was below 0.10 indicating excellent nanoassembly properties and monodisperse distribution. However, the NA size was influenced by the type of the building block. **Nano-*rac*-2** showed the biggest average size (130±2 nm), followed by **nano-*rac*-3** (115±5 nm) and **nano-*rac*-4** being the smallest (100±5 nm) as presented in Figure 2 and S19-S22. This is in line with reported examples of squalene conjugates where each construct shows different size distribution and topology features depending on the molecule conjugated to the squalene moiety.[22] Interestingly, **nano-*rac*-4** formed the smallest NAs. In construct **4** the squalene moiety is integrated into the [4]helicene core which presumably allows better packing and smaller NA size.

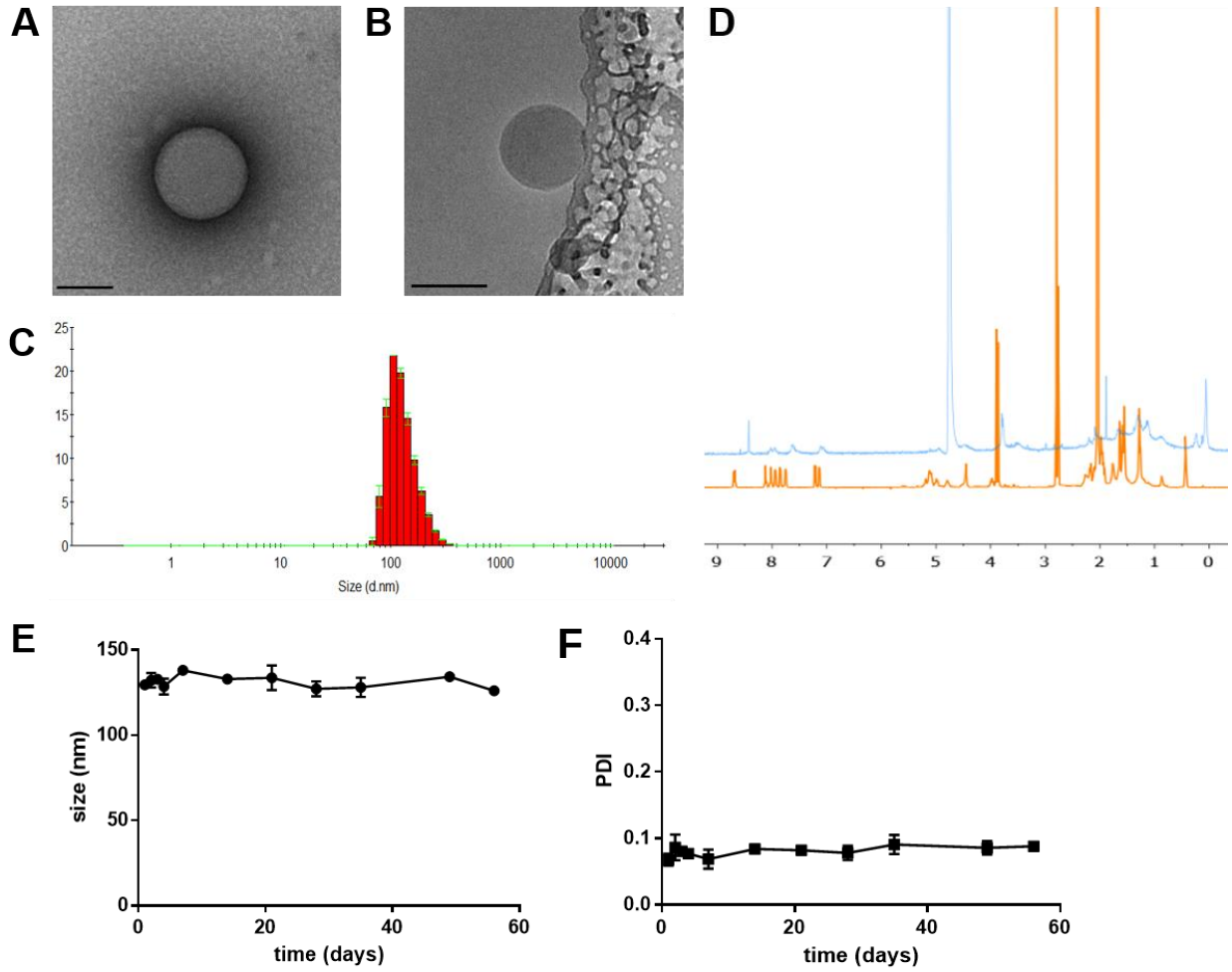

Figure 2. Characterization of **nano-*rac*-2**. TEM (A) and cryo-TEM image (scale 100 nm) (B) DLS size distribution showing (C), overlay of ^{1}H-NMR of **2** (orange) and **nano-*rac*-2** (blue) in deuterated acetone and water, respectively (D), and size (E)and PDI stability (F).

Reference diaza[4]helicene conjugates **10** and **11** containing C8 and C18 linear alkyl chains respectively, were used to test the building block requirements for good nanoassembly properties. Using the same nanoprecipitation procedure, NAs **nano-*rac*-10** and **nano-*rac*-11** were obtained respectively. However, the yield of the nanoassembly process differed drastically. The shorter aliphatic chain in derivative **10** resulted in NAs in less than 5% yield with most of the material precipitating out of the polar medium. On the other hand, **nano-*rac*-11** were obtained in excellent

yield with minimal losses comparable to the squalene series. As expected the apparent zeta potentials were strongly positive around +40 mV and the average size at 110 nm and PDI below 0.1, very similar to the squalene series **nano-*rac*-2-4** (Figures S25 and S26). These experiments demonstrated the importance long lipophilic chains such as squalene or stearyl that induce nanoassembly.

TEM and cryo-TEM experiments confirmed the range of the monodisperse size distribution established by DLS and revealed perfectly spherical morphology of the nanoparticles. Cryo-TEM of the **nano-*rac*-4** revealed a thin corona only a few nanometers in thickness around the nanoassembly visible at high magnifications (Figure 3). By cryo-TEM no higher order topologies such as lamellar[23] hexagonal liquid crystalline phase[24] or cubosomes[25] could be observed with any the NAs, most likely due to the very high lipophilicity of the nanoassembly building block conjugates.

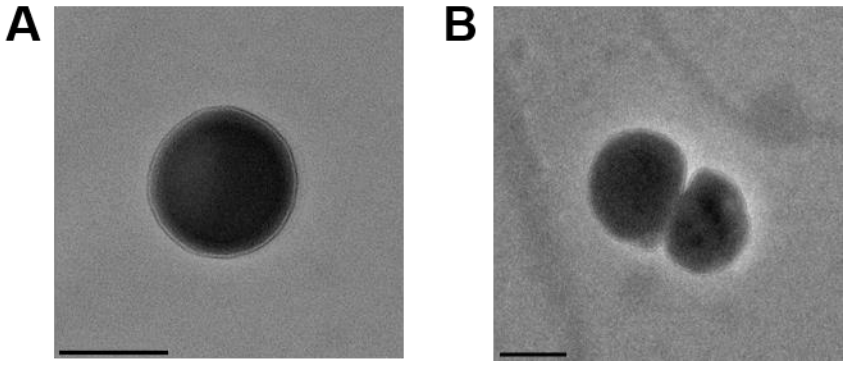

Figure 3. High magnification TEM (A) and cryo-TEM images (B) of **nano-*rac*-4**. Very thin corona measuring a few nm surrounding the nanoassemblies is visible in both images (scale 100 nm).

In an attempt to gain further insight into the nature of the new NAs, the nanoprecipitation was performed in deuterated water. After evaporation of the deuterated organic solvent we observed dramatic changes in ^{1}H NMR spectra in D_2O with water presaturation sequence. The peak broadening corroborated the presence of nanoassemblies in D_2O. The squalene protons are predictably broad due to the supramolecular structures present in D_2O (Figure 3D and S20).

For all NAs the apparent zeta potential was found positive at +37 ± 1 mV. The positive charge of the nanoparticles is a consequence of the positive charge of the helicene cation building block. The same apparent zeta potential is also partially responsible for the impressive stability of the nano systems. Figure 2E and 2F demonstrate stability over a period of 2 months. Both average size and PDI remained practically constant during this period. **Nano-*rac*-3** and **nano-*rac*-4** display similar stability profiles (Figures S21 and S22).

NAs were prepared using ***M*–2** and ***P*–2** and DLS analysis revealed that both enantiomers showed smaller size average diameter, with 90±1 nm and 99±5 nm for **nano-*M*–2** and ***P*–2**, respectively (Figures S23 and S24). Compared to the size distribution of **nano-*rac*-2**, which showed a larger size average of 126±7 nm, these values indicate a better packing of enantiopure building blocks within the NAs. This observation is interesting in view of the stronger aggregation in water of racemic DMQAs **1** (R = Me, Pr) in comparison to their enantiopure equivalents.[26]

Optical and chiroptical properties

The optical properties have been recorded for **2-4** single molecular entities (non-nanoassembled building blocks) in acetonitrile and for **nano-*rac*-2-4** NA in water (**Table 1**). The absorption spectra of the NAs are presented in Figure 4A. They show intense absorption in the orange-red region of the visible spectrum, with maxima centered at 594, 608 and 618 nm, for ester-derivative **2**, amide-

derivative **3** and integrated squalene-DMQA composite **4**, respectively. The fluorescence is centered in the red range *ca.* 660 nm for the three types of NAs, with average Stokes shifts of 1350-1550 cm^{-1} and cut-off emissions reaching the NIR region, up to 800 nm. The absorption and fluorescence profiles recorded for **2**-**4** as single molecules in acetonitrile or as NAs are quasi-superimposable, however a noticeable 8 nm red-shift is observed for **nano-*rac*-4** emission band (Figures S15-16).

Table 1. Optical data of racemic diaza [4]helicenes (acetonitrile) and corresponding racemic NAs (water).

Compound	λ_{max} / nm (ε_{max} / $L.mol^{-1}.cm^{-1}$)	λ_{em} / nm	Φ [a]	τ_1 / ns [b]	τ_2 / ns [b]
2	592 (11,100)	654	0.39	14.7	-
nano-*rac*-2	594	654	0.13	7.3 (68%)	12.3 (32%)
3	609 (10,800)	666	0.20	8.9	-
nano-*rac*-3	608	662	0.07	4.9 (76%)	9.0 (24%)
4	616 (4,920)	668	0.10	4.6	-
nano-*rac*-4	618	676	0.03	1.7 (82%)	5.5 (18%)
11	593 (12,600)	653	0.34	14.1	-
nano-*rac*-11	591	687	0.04	2.4	-

[a] Relative to cresyl violet (Φ = 0.54 in MeOH). [b] NanoLED excitation at 570 nm, composition indicated in parentheses.

In general, the fluorescence quantum yields are significantly impacted by the solvent and the organization of the dye. In the instance of **2**, an honourable fluorescence efficiency of 0.39 is recorded in acetonitrile, which drops to 0.13 for the corresponding **nano-*rac*-2** NAs in aqueous medium. Such quench of the fluorescence in polar solvent is classically accompanied with an

enhancement of non-radiative de-excitation. It is furthermore worthy to underline that a progressive decrease of the fluorescence quantum yield and lifetime values occurs as the emission maxima are red-shifted (ϕ(**2**) > ϕ(**3**) > ϕ(**4**)), as previously observed.[17a] Fluorescence time profiles reveal non-negligible emission lifetimes for organic red-fluorophores in acetonitrile, with values comprised between 14.7 ns and 4.6 ns, respectively for **2** and **4** in acetonitrile. Bi-exponential fits were necessary in order to determine the lifetimes of the NAs in water, which is the signature of two different emissive species, presumably corresponding to excited single molecules or excited aggregates that could partially quench the fluorescence.[15]

The electronic circular dichroism (ECD) spectra of both enantiomers of **2** and **nano-2** were respectively recorded in acetonitrile and milli-Q water, and the spectra are compared in Figure 4B (peak values are reported in the Supporting Information). Enantiomers *M*–**2** and *P*–**2** display mirror spectra characterized by strong Cotton effect in the UV region with peaks at 214 and 301 nm ($|\Delta\varepsilon|$ *ca.* 40 $M^{-1}.cm^{-1}$) and less intense transitions in the visible range centered *ca.* 460 and 600 nm.

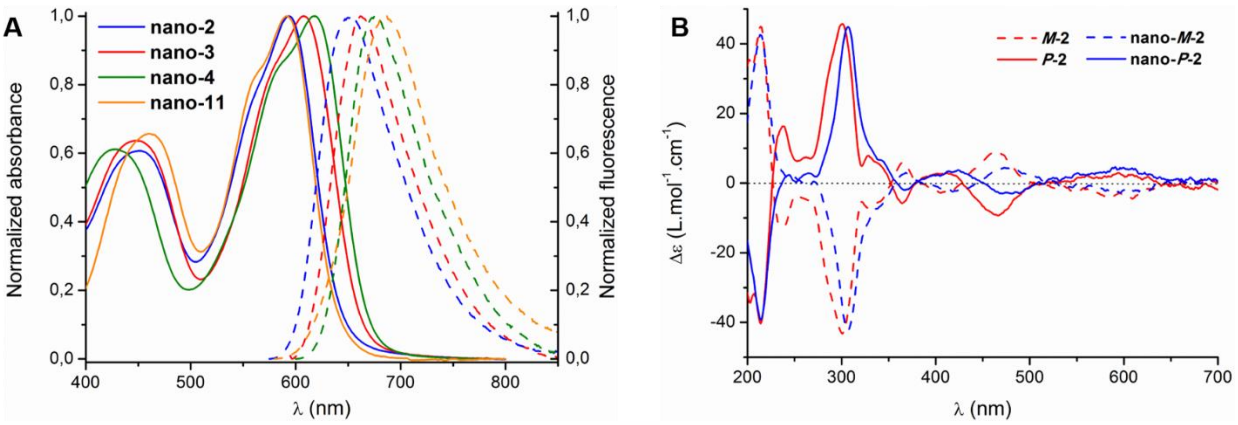

Figure 4. Normalized absorption (plain lines) and fluorescence (dashed lines) spectra of racemic NAs in water (A) and UV-vis electronic circular dichroism spectra of *M*–**2** (dashed lines) and *P*–**2** (plain lines) single molecules (acetonitrile, red) and NAs (H_2O, blue) (B).

The lower energy band remains unchanged in the case of enantiopure **nano-*M*/*P*–2**, whereas a distinct bathochromic shift of 10 nm is observed for the ECD signals around 310, 415 and 470 nm. Interestingly, these red-shifted transitions are only slightly detected between the absorption spectra of enantiopure *M*/*P*–**2** and **nano-*M*/*P*–2** (Table S1, Figure S17).

Cell imaging

As mentioned, helicenes are rarely used in bioimaging due, in general, to poor water solubility, acute toxicity and suboptimal optical properties. However, constructs **2-4** seemed ideal to solve of these problems as (i) ester or amide groups on the [4]helicene core leads to brighter derivatives ($\varepsilon.\phi$ = 4'220 $M^{-1}.cm^{-1}$ for **2**)[17a] and (ii) the linkage of squalene or other extended aliphatic chains prolongs further the fluorescence into the far-red windows and permits the formation of nanoassemblies. The latter properties allows the transfer of highly lipophilic dyes into aqueous media, thus greatly facilitating bioimaging applications.[27]

Hence, all the prepared NAs could be easily screened by incubation with cancer cells using high-throughput screening platform. It became immediately apparent that the staining pattern was specific for a sub-cellular organelle in HeLa cells. Co-staining with MitoTracker Green revealed excellent overlap and confirmed the highly specific staining of mitochondria by NAs. As shown in Figure 6, this is the case for **nano-*rac*-2** and both enantiopure **nano-*M*–2** and **nano-*P*–2** with small differences in staining pattern between these NAs. Similar specificity was observed for **nano-*rac*-3**, but interestingly, **nano-*rac*-4** stained mitochondria with a lower affinity (Figure S27 and S28, respectively). The specific sub-cellular mitochondrial accumulation and staining is a consequence of the physico-chemical properties of the building blocks, the nature of the linkage

that attaches the squalene chains to the helical core, but not of the stereochemical nature of the helicene (*rac*, *M* or *P*).

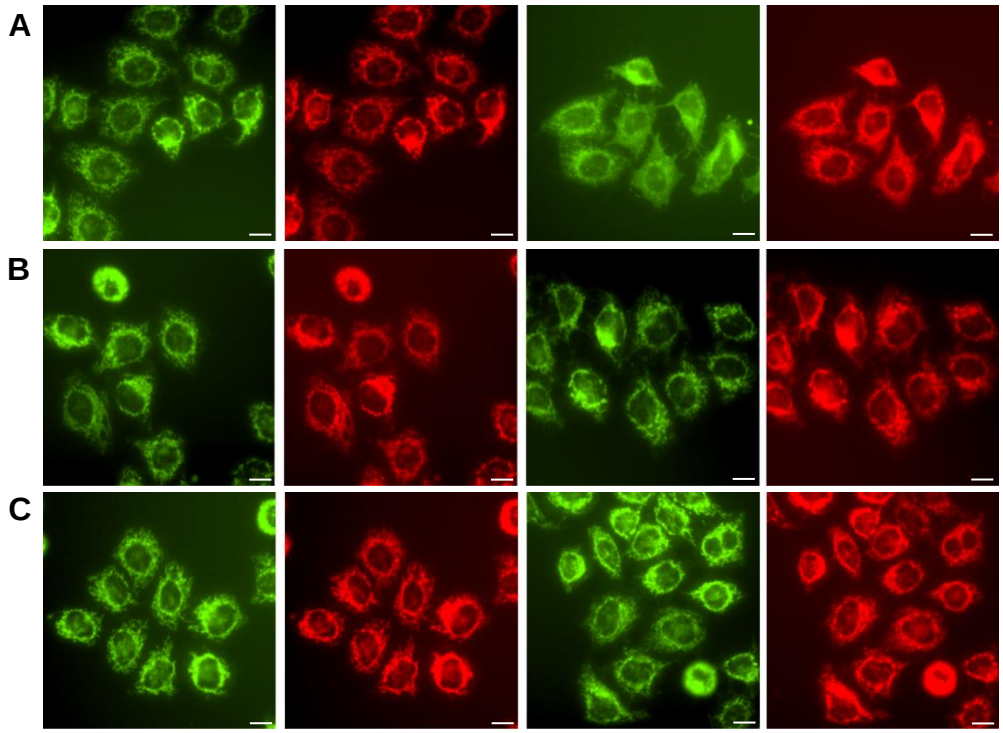

Figure 6. High-throughput imaging of racemic and chiral NAs on HeLa cells. NAs in water (left) and equivalent DMSO solutions (right). Racemic **nano-2** (A), **nano-*M*–2** (B) and **nano-*P*–2** (C). Mitochondria labelled with MitoTracker (green) and NA (red). NA concentration 1 μM. Scale bar (10 μm).

Diaza [4]helicenes could be then potentially considered as a new member of structural class called delocalized lipophilic cations (DLC). They are known to accumulate in mitochondria due to high negative potential of the mitochondrial inner membrane caused by the electron transport chain and proton flux across the membrane.[28] Only a handful of DLCs are routinely used to label mitochondria today namely, 5,5',6,6'-tetrachloro-1,1',3,3'-tetraethylbenzimidazol-carbocyanine iodide (JC-1), Rhodamine-123, and Mitotracker.[29] Triphenyl phosphonium is non-fluorescent DLC and has been used as a mitochondrial targeting ligand.[30] The passive transport of DLCs into mitochondria is energetically favorable because of the charge delocalization creating a much greater ionic radius and the effectively lowering enthalpy of desolvation upon transfer into lipid

environment. The result can be several 100-fold higher concentrations of cations in the mitochondria compared to outside of the cells.[31]

Additional imaging experiments with several control compounds gave us more insight in the structure-activity relationship. As expected and previously reported,[26] unfunctionalized DMQA cation **1** (Chart 1, A) displayed non-specific mostly nuclear DNA staining (Figure S32). On the other hand and importantly, the linear aliphatic conjugate DMQA-C_{18} **11** that displayed good nanoassembly properties with similar average sizes and PDI, surprisingly did not display the same cell staining pattern as the squalene series. The staining of **nano-*rac*-11** was weaker, spotty and mitochondria non-specific (Figure 7). The major difference between DMQA-C_{18} **nano-11** and the squalene series **nano-1-3** is the presence of multiple substituted double bonds in squalene which display the $A^{1,3}$ strain driving the squalene moiety into a folded conformation compared to the predominantly linear C_{18} chains. The mitochondrial specificity of the constructs is therefore inherent to the whole construct and not the individual squalene or helicene parts.

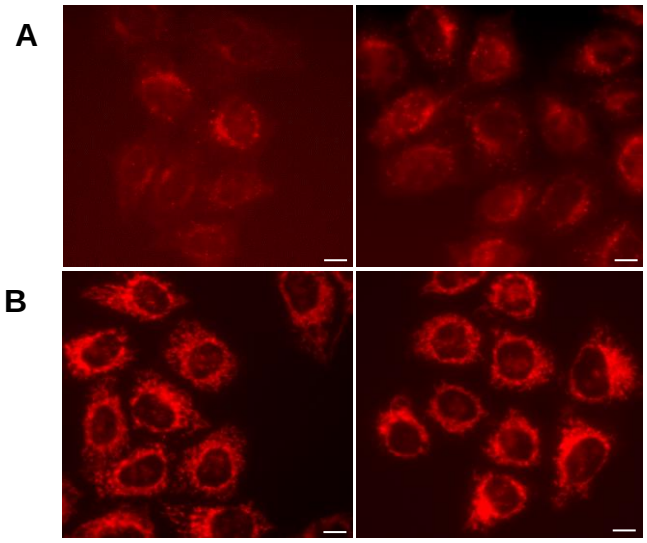

Figure 7. High-throughput imaging of [4]helicene-C18 **nano-11** control (A) and racemic **nano-2** (B) on HeLa cells. NAs (left) and equivalent DMSO solutions (right). NA concentration 1 μM. Scale bar (10 μm).

LogP of **nano-*rac*-2** and **nano-*rac*-11** were calculated at 11.6 and 10.4 respectively, which is more than 10 orders of magnitude higher than logP of Rhodamine-123, a prototypical mitochondrial dye.[32] It is very surprising that very high lipophilicity of the squalene NAs **2-4** did not bring about any considerable membrane accumulation as previously reported for other squalene NAs, such as squalenoyl gemcitabine (Chart 1). Squalene prodrugs normally distribute within cellular membranes, including those of organelles such as endoplasmatic reticulum.[33] It would be expected that with logP values of this order of magnitude the lipophilic partitioning overrides the delocalized cationic character of the compounds. However, this is clearly not the case for **nano-*rac*-2** (Figure 7). Intracellular phenomena governing the distribution of this type of squalene NAs are not yet understood and deserve further investigations.

Internalization kinetics

Couvreur and co-workers presented evidence for another important aspect of squalene-based NAs. They demonstrated that squalenoyl gemcitabine NAs did not enter the cell through endocytosis but as single building block molecules by passive diffusion.[34] This is perhaps the most striking difference of squalene based systems compared to other types of nanoparticles.[35] The internalization studies usually require the use of fluorescent probes integrated into the nanoconstructs. Our nanosystems allowed the use of inherent NA fluorescence to follow and study internalization kinetics in several cell lines. In both U87MG and PC3 cell lines very fast internalization was observed. Confocal scanning microscopy revealed detectable amounts of NAs even after only 10 min of incubation at 37 °C and considerable amounts of the NAs in 30 min (Figure 8C and S29). The rapid kinetics of internalization and the absence of endosome-like

vesicular structures confirms the passive internalization mechanism of single building blocks rather than the full NAs. This was further confirmed by preparing solutions of the building blocks **2**, ***M*-2** and ***P*-2** in DMSO, diluting them in cell media and incubating them with HeLa cells. The mitochondrial staining was practically identical as with NAs. Active vs. passive internalization mechanism was further investigated by incubation of HeLa cells with **nano-*M*-2** at 37 and 4 °C. The result shows fluorescence labeling of HeLa cells occurs at both temperatures, although the labeling is stronger at 37 °C. The experiment validates passive mechanism of internalization by diffusion of individual molecules into the cells.

Confocal microscopy also allowed the quantification of co-localization. Pearson co-localization coefficient was determined for **nano-*M*-2** at 0.79 for PC3 and U87MG cells at 30 min (Figures S30 and S31, respectively).

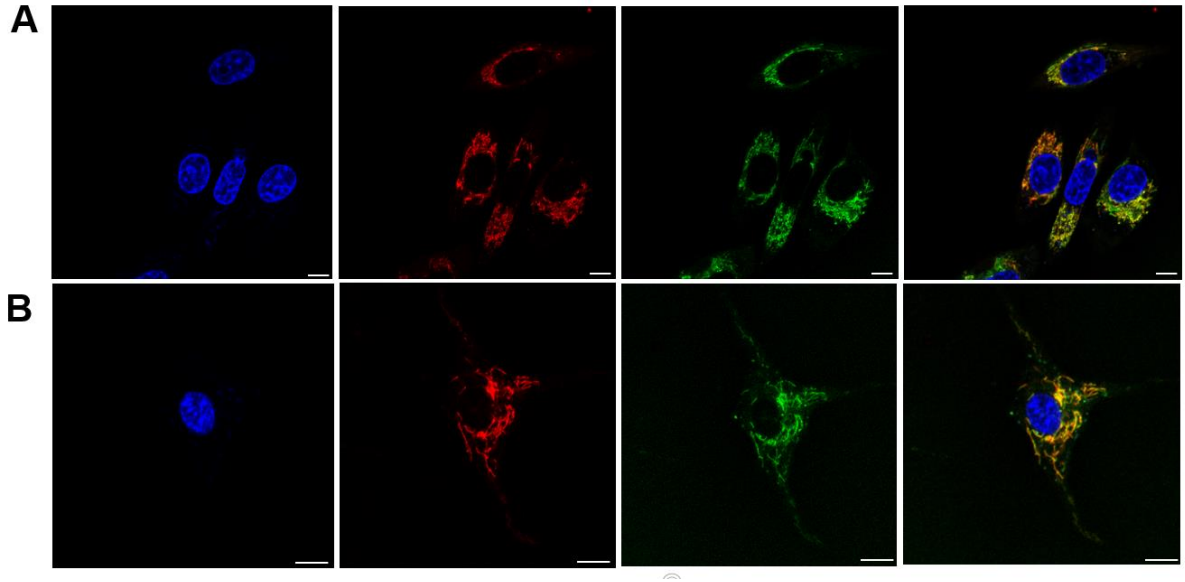

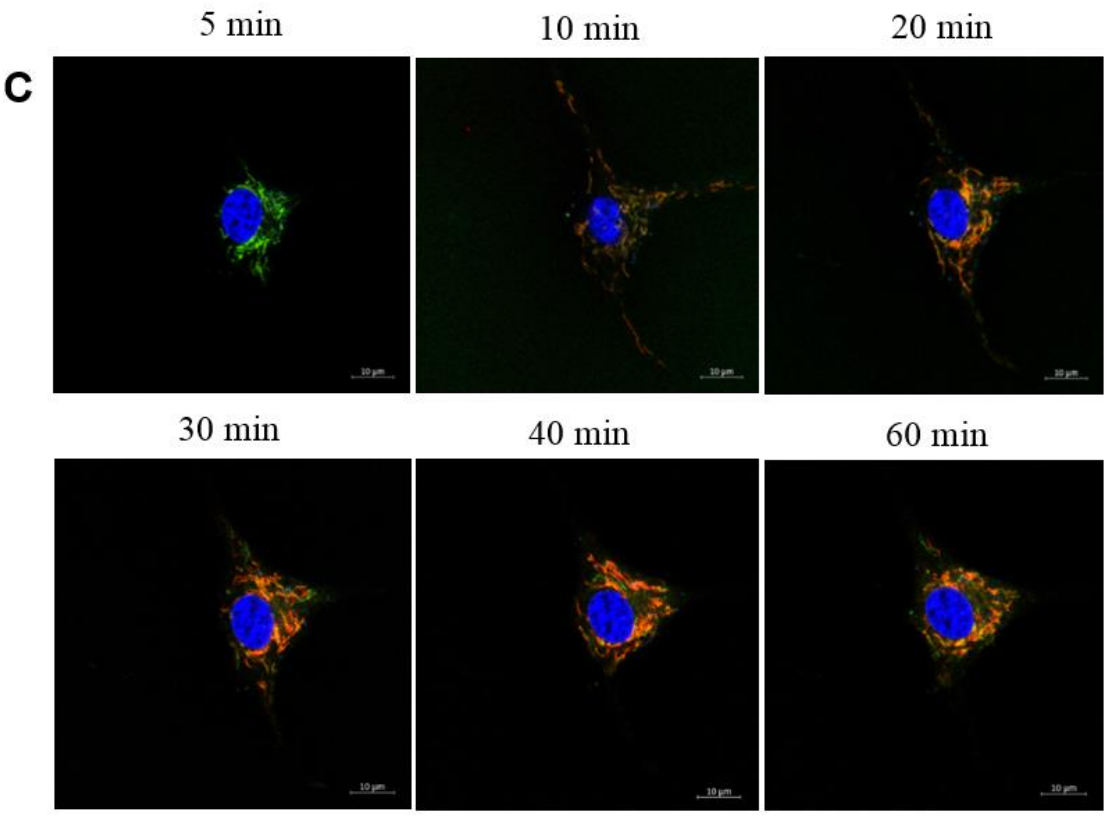

Figure 8. Live-cell imaging by confocal laser scanning microscopy of **nano-*M*-2** with PC3 prostate cancer cells (A) and U87MG glioblastoma cells (B) after 20 min of incubation. Left to right, cell nuclei (blue), mitochondria stained with MitoTracker (green), and **nano-*M*-2** (red), and overlay (scale bar 10 μm). Cell internalization kinetics of **nano-*M*-2** at 5, 10, 20, 30, 40 and 60 min of incubation in U87MG (C). Excellent mitochondrial staining upon rapid uptake of the probe was observed in both cell lines. NA concentration was 1 μM.

Cytotoxicity

Cell viability of the most promising NAs **nano-*rac*-2** and enantiopure **nano-*M*-2** was determined to assess their biocompatibility. HeLa cells were incubated with 10, 1.0, 0.1 and 0.01 μM concentrations of NAs for 2 h, 6 h, and 24 h. Considerable cytotoxicity was detected only at 10 μM and 24h incubation time (Figure S33). It is noteworthy that **nano-*rac*-11** control displayed lower cytotoxicity than **nano-*rac*-2** at the same concentration.

CONCLUSIONS

In conclusion, this study presents the squalenoylation of lipophilic diaza[4]helicene dyes. In aqueous solution, the stable monodisperse NAs displayed effective brightness in the transparency window of biological media and impressive mitochondrial accumulation in several cell lines. To the best of our knowledge, this is the first example of squalene-based nanoassembly system that demonstrates the feasibility of specific sub-cellular targeting. In light of the emerging central role of mitochondria in the regulation of cellular signaling, homeostasis, and apoptosis with major implications for cancer and other diseases, novel nano-platforms with mitochondrial targeting properties show great promise in theranostic nanomedicine.

METHODS

General. Column chromatography was performed using Siliaflash P60 silicagel (40-63 μm, 60 Å) and Acros Brockmann I basic alumina (40-200 μm, 60 Å). Optical properties were recorded in analytical grade acetonitrile and Milli-Q water (specific resistance 18.2 MΩcm @ 25 °C). NMR spectra were recorded on Brucker Avance II+ AMX-500 and Varian Anova 500 MHz spectrometers at room temperature. NMR chemical shifts are given in ppm (δ) relative to Me_4Si with solvent resonances used as internal standards (CD_2Cl_2: 5.32 ppm for ^1H and 53.8 for ^{13}C). IR spectra were recorded on a Perkin-Elmer 1650 FT-IR spectrometer using a diamond ATR Golden Gate sampling. Melting points (M.P.) were measured in open capillary tubes with a Buchi B-550 melting points apparatus and are uncorrected. UV-vis-NIR absorption spectra were recorded on a JASCO V-650 spectrophotometer at 20°C. Electrospray mass spectra were obtained on a Finnigan SSQ 7000 spectrometer QSTAR pulsar i (AB / MDS Sciex), ESI (TIS)/nanoESI/APCI-QqTof by the Mass Spectroscopy Platform of the Faculty of Sciences, University of Geneva. Optical rotation were measured on a Perkin Elmer 241 polarimeter at 20°C using a Hg lamp (365 nm). Electronic circular dichroism spectra were recorded on a JASCO J-815 spectrophotometer at 20°C. LogP was calculated using Chemicalize software and Marvin JS editor.

Luminescence. Steady-state fluorescence spectra were measured using a Varian Cary 50 Eclipse spectrofluorimeter. All fluorescence spectra were corrected for the wavelength-dependent sensitivity of the detection. Fluorescence quantum yields Φ were measured in diluted solution with an optical density lower than 0.1 using the following equation:

$$\frac{\Phi_x}{\Phi_r} = \left(\frac{\mathrm{A}_r(\lambda)}{\mathrm{A}_x(\lambda)}\right)\left(\frac{n_x^2}{n_r^2}\right)\left(\frac{\mathrm{D}_x}{D_r}\right)$$

where A is the absorbance at the excitation wavelength (λ), n the refractive index and D the integrated intensity. “r” and “x” stand for reference and sample. The fluorescence quantum yields were measured relative to cresyl violet in methanol (Φ = 0.54). Excitation of reference and sample compounds was performed at the same wavelength. Short luminescence decay was monitored with the TC-SPC Horiba apparatus using Ludox in distilled water to determine the instrumental response function used for deconvolution. Excitation was performed using a 570 nm NanoLED (peak wavelength: 573 nm; pulse duration: 1.5 ns), and the deconvolution was performed using the DAS6 fluorescence-decay analysis software.

Preparation of nanoassemblies Compound (1.00 μmol) was dissolved in a 50/50 V/V mixture acetone/ethanol (500 μL). The organic phase was added dropwise using a micro-syringe into MilliQ water (1.25 mL) at 100 μL/min under stirring. After 5 min under stirring the magnetic stir bar was removed and the organic solvents and the excess of water removed using a rotary evaporator at 40 °C. The evaporation program was the following: 5 min at 400 mbar, 5 min at 200 mbar, 10 min at 100 mbar and the remaining time at 80mbar. The final concentration of nanoassemblies was 1.00 mM**.**

Characterisation of Nanoassemblies. Hydrodynamic diameters of nanoassemblies were measured by dynamic light scattering (DLS) using a NANO ZS instrument from Malvern (Worcestershire, UK) running the ZetaSizer 7.01 software. The analyses were performed with 4 mW He-Ne Laser (633 nm) at scattering angle of 173° at 25 °C in Polystyrene (PS) micro cuvette from Brand (Wertheim, Germany). Zeta potential (ZP) was determined using the same Nano ZS instrument from Malvern in folded capillary cells DTS 1070 from Malvern. Size distribution and size mean diameter were calculated from the data.

The morphological examination of nanoassemblies was performed using a transmission electron microscope (TEM) instrument TECNAI® G^2 Sphera (FEI, Thermo Fisher Scientific) equipped with 2000 by 2000 pixel high resolution digital camera TCL (Gräfelfing, Germany). Samples were negatively stained with uranyl 2 % on a carbon film 200 Hex Mesh copper grid and run at 200 kV with a LaB6 cathode.

For the cryogenic transmission electron microscope (cryo-TEM) the vitrified-ice samples were prepared using the Virtobot cryo-plunger (FEI, Thermo Fisher Scientific). 2.0 μL of nanoassemblies (1.0 mM) were applied to Quantifoil Cu/Rh 200 mesh R3.5/1 grids (SPI, West Chester, USA) and vitrified using liquid ethane.

NMR of Nanoassemblies in Deuterated Water. The nanoassemblies were prepared as described above except that deuterated solvents were used. The initial solution of the nanoassembly material in deuterated acetone was recorded at 500 MHz first. After the nanoprecipitation the spectra were recorded in D_2O. The HDO signal was suppressed using presaturation before running the ^1H sequence.

Stability. The stability of nanoassemblies was monitored by visual control and by the change in particle size by dynamic light scattering upon storage at room temperature during a 2 months period in the dark. PDI and average size were recorded for each time point.

High-throughput imaging. HeLa cell maintenance and imaging were performed has described by Wallabregue et al.[36] and Chuard et al. (REF) The automated IXM-XL microscope from molecular devices™ has been used to ensure consistent imaging conditions between all the samples. Fluorescent images were acquired with a 40X objective using the appropriate filter cube (405nm, 488nm and 594nm). Nanoassemblies were incubated at 1.0 µM concentration and equivalent DMSO solutions were prepared by diluting 2.0 mM DMSO solution to 1.0 µM with cell media.

Cell viability. The cell viability assay has been performed with the same automated IXM-XL microscope from molecular devices™. The HeLa cells have been treated for the time and concentration described in the manuscript in 96 well plate, with 4 replicates per condition. Once fixed with PFA the nuclei have been stained with Hoechst. Using MetaXpress™ software each individual nucleus has been segmented and counted. The cell viability is directly reflect by the count of viable nuclei compared to control cells without NAs.

Confocal scanning microscopy. U87MG human glioblastoma cancer cells (ATTC® HTB-14™, Manassas, Virginia) and PC3 human prostate cancer cells (ATTC® CRL-1435™, Manassas, Virginia) were maintained in MEM (U87MG) and F12K nutrient mix (PC3). Culture media were supplemented with 10% fetal calf serum (CVFSVF00-01, Eurobio) and 100 µl/ml streptomycin and 100 IU/ml penicillin (15140-122, Thermo Fisher Scientific). The cells were seeded into ibidi µ-Slides, ibiTreat, 4 (80426-IBI) or 8 (80826-IBI) wells 24 h before the experiments. Hoechst 33342 (2 µg/mL, Thermo Fisher Scientific) and MitoTracker green (50 nM, M7514 Thermo Fisher Scientific) were freshly prepared in incomplete culture medium before imaging. Cell monolayers in each well were incubated at 37 °C with the solution of Hoechst and MitoTracker Green (700 µL) for 30 min. The cells were washed 2 times with DPBS. The cells were then incubated with nanoassemblies at 1.0 µM and imaged at regular time points at different locations within the wells. Control cells were incubated in complete culture medium under the same experimental conditions. Detection and localization of fluorescence in cells was done with the Zeiss LSM780 (Jena, Germany) inverted confocal microscope fitted with an objective lens Plan-Aprochromat 63 x/1.4 oil DIC M27. The images were taken using 405 nm, 488 nm and 590 nm excitation lasers and 430-470 nm, 500-550 nm, 680-800 nm emission band filters respectively. During the image acquisition time, slides were kept at 37 °C and 5% of CO_2 in a humidified chamber (INUBTF-WSKM-F1, Tokai Hit, Gendoji-cho, Fujinomiya-shi, Shizuoka-ken, Japan). ZEN 2 software (Zeiss, Jena, Germany) was used for image processing.

Co-localization quantification. Quantification of co-localization between NAs (red) and MitoTracker® Green was done by determining Pearson's coefficient of correlation (PCC) with Imaris x 64 8.0.0 software. PCC values may range between +1 (perfect correlation) and -1 (perfect negative correlation), where 0 means no correlation.[37] Regions of interest (ROI) were defined and PCC was calculated. ROI was defined for each image separately by masking the dataset with red channel (NAs fluorescence). The value of PCC for each experiment is presented as means ± s.d. calculated from 3 separate images.

Statistical analysis. Statistical analysis were performed with Graphpad Prism 6.05 using the Student's t-test. Data with $p < 0.05$ were considered statistically significant.

ASSOCIATED CONTENT

Supporting Information Available:

AUTHOR INFORMATION

Corresponding Authors

*andrej.babic@unige.ch, jerome.lacour@unige.ch, eric.allemann@unige.ch.

Author Contributions

The manuscript was written through contributions of all authors. All authors have given approval to the final version of the manuscript.

Funding Sources

Any funds used to support the research of the manuscript should be placed here (per journal style).

Notes

All of the authors declare no conflict of interest.

Acknowledgement

We thank Dr. Christoph Bauer and Jérôme Bosset from the Bioimaging platform at the University of Geneva for their input and help in live cell imaging. We are grateful to Dr. Laurence Marcourt of the School of Pharmaceutical Sciences Geneva-Lausanne for her contribution in NMR experiments. We thank the "Laboratoire de Chimie" at the ENS Lyon for access to NanoLED and TS-SPC equipment. We would also like to acknowledge the Mass Spectrometry platform at the University of Geneva for the mass spectroscopy analysis. We thank Canton of Geneva, Switzerland and Swiss National Science Foundation for funding.

REFERENCES

1. (a) Nie, Z. H.; Petukhova, A.; Kumacheva, E. Properties and emerging applications of self-assembled structures made from inorganic nanoparticles. *Nat Nanotechnol* **2010,** *5* (1), 15-25; (b) Grzelczak, M.; Vermant, J.; Furst, E. M.; Liz-Marzan, L. M. Directed self-assembly of nanoparticles. *Acs Nano* **2010,** *4* (7), 3591-605.
2. Arias, J. L.; Reddy, L. H.; Othman, M.; Gillet, B.; Desmaele, D.; Zouhiri, F.; Dosio, F.; Gref, R.; Couvreur, P. Squalene Based Nanocomposites: A New Platform for the Design of Multifunctional Pharmaceutical Theragnostics. *Acs Nano* **2011,** *5* (2), 1513-1521.
3. Reddy, L. H.; Couvreur, P. Squalene: A natural triterpene for use in disease management and therapy. *Advanced drug delivery reviews* **2009,** *61* (15), 1412-26.
4. (a) Maksimenko, A.; Dosio, F.; Mougin, J.; Ferrero, A.; Wack, S.; Reddy, L. H.; Weyn, A. A.; Lepeltier, E.; Bourgaux, C.; Stella, B.; Cattel, L.; Couvreur, P. A unique squalenoylated and nonpegylated doxorubicin nanomedicine with systemic long-circulating properties and anticancer activity. *Proceedings of the National Academy of Sciences of the United States of America* **2014,** *111* (2), E217-26; (b) Desmaele, D.; Gref, R.; Couvreur, P. Squalenoylation: A generic platform for nanoparticular drug delivery. *J Control Release* **2012,** *161* (2), 609-618.
5. Lepeltier, E.; Bourgaux, C.; Rosilio, V.; Poupaert, J. H.; Meneau, F.; Zouhiri, F.; Lepetre-Mouelhi, S.; Desmaele, D.; Couvreur, P. Self-assembly of squalene-based nucleolipids: relating the chemical structure of the bioconjugates to the architecture of the nanoparticles. *Langmuir : the ACS journal of surfaces and colloids* **2013,** *29* (48), 14795-803.
6. Maksimenko, A.; Alami, M.; Zouhiri, F.; Brion, J. D.; Pruvost, A.; Mougin, J.; Hamze, A.; Boissenot, T.; Provot, O.; Desmaele, D.; Couvreur, P. Therapeutic modalities of squalenoyl nanocomposites in colon cancer: an ongoing search for improved efficacy. *Acs Nano* **2014,** *8* (3), 2018-32.
7. (a) Fan, G.; Lin, Y. X.; Yang, L.; Gao, F. P.; Zhao, Y. X.; Qiao, Z. Y.; Zhao, Q.; Fan, Y. S.; Chen, Z.; Wang, H. Co-self-assembled nanoaggregates of BODIPY amphiphiles for dual colour imaging of live cells. *Chem Commun (Camb)* **2015,** *51* (62), 12447-50; (b) Xing, P.; Chen, H.; Bai, L.; Zhao, Y. Photo-triggered transformation from vesicles to branched nanotubes fabricated by a cholesterol-appended cyanostilbene. *Chem Commun (Camb)* **2015,** *51* (45), 9309-12; (c) Wu, Y.; Huang, S.; Zeng, F.; Wang, J.; Yu, C.; Huang, J.; Xie, H.; Wu, S. A ratiometric fluorescent system for carboxylesterase detection with AIE dots as FRET donors. *Chem Commun (Camb)* **2015,** *51* (64), 12791-4.
8. Zhang, H.; Ma, X.; Nguyen, K. T.; Zhao, Y. Biocompatible pillararene-assembly-based carriers for dual bioimaging. *Acs Nano* **2013,** *7* (9), 7853-63.
9. Lovell, J. F.; Jin, C. S.; Huynh, E.; Jin, H. L.; Kim, C.; Rubinstein, J. L.; Chan, W. C. W.; Cao, W. G.; Wang, L. V.; Zheng, G. Porphysome nanovesicles generated by porphyrin bilayers for use as multimodal biophotonic contrast agents. *Nat Mater* **2011,** *10* (4), 324-332.
10. Guo, Z.; Park, S.; Yoon, J.; Shin, I. Recent progress in the development of near-infrared fluorescent probes for bioimaging applications. *Chemical Society Reviews* **2014,** *43* (1), 16-29.
11. (a) Shen, Y.; Chen, C. F. Helicenes: synthesis and applications. *Chem Rev* **2012,** *112* (3), 1463-535; (b) Gingras, M.; Felix, G.; Peresutti, R. One hundred years of helicene chemistry. Part 2: stereoselective syntheses and chiral separations of carbohelicenes. *Chem Soc Rev* **2013,** *42* (3), 1007-50.

12. (a) Amemiya, R.; Yamaguchi, M. Chiral recognition in noncovalent bonding interactions between helicenes: right-handed helix favors right-handed helix over left-handed helix. *Organic & Biomolecular Chemistry* **2008,** *6* (1), 26-35; (b) Qu, X.; Trent, J. O.; Fokt, I.; Priebe, W.; Chaires, J. B. Allosteric, chiral-selective drug binding to DNA. *Proceedings of the National Academy of Sciences* **2000,** *97* (22), 12032-12037; (c) Honzawa, S.; Okubo, H.; Anzai, S.; Yamaguchi, M.; Tsumoto, K.; Kumagai, I. Chiral recognition in the binding of helicenediamine to double strand DNA: interactions between low molecular weight helical compounds and a helical polymer. *Bioorganic & Medicinal Chemistry* **2002,** *10* (10), 3213-3218; (d) Xu, Y.; Zhang, Y. X.; Sugiyama, H.; Umano, T.; Osuga, H.; Tanaka, K. (P)-Helicene Displays Chiral Selection in Binding to Z-DNA. *Journal of the American Chemical Society* **2004,** *126* (21), 6566-6567; (e) Passeri, R.; Aloisi, G. G.; Elisei, F.; Latterini, L.; Caronna, T.; Fontana, F.; Sora, I. N. Photophysical properties of N-alkylated azahelicene derivatives as DNA intercalators: counterion effects. *Photochemical & Photobiological Sciences* **2009,** *8* (11), 1574-1582; (f) Latterini, L.; Galletti, E.; Passeri, R.; Barbafina, A.; Urbanelli, L.; Emiliani, C.; Elisei, F.; Fontana, F.; Mele, A.; Caronna, T. Fluorescence properties of aza-helicenium derivatives for cell imaging. *Journal of Photochemistry and Photobiology A: Chemistry* **2011,** *222* (2–3), 307-313; (g) Kel, O.; Fürstenberg, A.; Mehanna, N.; Nicolas, C.; Laleu, B.; Hammarson, M.; Albinsson, B.; Lacour, J.; Vauthey, E. Chiral Selectivity in the Binding of [4]Helicene Derivatives to Double-Stranded DNA. *Chemistry – A European Journal* **2013,** *19* (22), 7173-7180.
13. Selvaraju, R. K.; Velikyan, I.; Asplund, V.; Johansson, L.; Wu, Z. H.; Todorov, I.; Shively, J.; Kandeel, F.; Eriksson, B.; Korsgren, O.; Eriksson, O. Pre-clinical evaluation of [Ga-68]Ga-DO3A-VS-Cys(40)-Exendin-4 for imaging of insulinoma. *Nucl Med Biol* **2014,** *41* (6), 471-476.
14. (a) Laursen, B. W.; Krebs, F. C. Synthesis of a Triazatriangulenium Salt. *Angewandte Chemie International Edition* **2000,** *39* (19), 3432-3434; (b) W. Laursen, B.; C. Krebs, F. Synthesis, Structure, and Properties of Azatriangulenium Salts. *Chemistry – A European Journal* **2001,** *7* (8), 1773-1783; (c) Herse, C.; Bas, D.; Krebs, F. C.; Bürgi, T.; Weber, J.; Wesolowski, T.; Laursen, B. W.; Lacour, J. A Highly Configurationally Stable [4]Heterohelicenium Cation. *Angewandte Chemie International Edition* **2003,** *42* (27), 3162-3166.
15. Kel, O.; Sherin, P.; Mehanna, N.; Laleu, B.; Lacour, J.; Vauthey, E. Excited-state properties of chiral [4]helicene cations. *Photochemical & Photobiological Sciences* **2012,** *11* (4), 623-631.
16. Laleu, B.; Mobian, P.; Herse, C.; Laursen, B. W.; Hopfgartner, G.; Bernardinelli, G.; Lacour, J. Resolution of [4]Heterohelicenium Dyes with Unprecedented Pummerer-like Chemistry. *Angewandte Chemie* **2005,** *117* (12), 1913-1917.
17. (a) Delgado, I. H.; Pascal, S.; Wallabregue, A.; Duwald, R.; Besnard, C.; Guenee, L.; Nancoz, C.; Vauthey, E.; Tovar, R. C.; Lunkley, J. L.; Muller, G.; Lacour, J. Functionalized cationic [4] helicenes with unique tuning of absorption, fluorescence and chiroptical properties up to the far-red range. *Chem Sci* **2016,** *7* (7), 4685-4693; (b) Pascal, S.; Besnard, C.; Zinna, F.; Di Bari, L.; Le Guennic, B.; Jacquemin, D.; Lacour, J. Zwitterionic [4] helicene: a water-soluble and reversible pH-triggered ECD/CPL chiroptical switch in the UV and red spectral regions. *Org Biomol Chem* **2016,** *14* (20), 4590-4594.
18. Sørensen, T. J.; Nielsen, M. F.; Laursen, B. W. Synthesis and Stability of N,N′-Dialkyl-1,13-dimethoxyquinacridinium (DMQA+): A [4]Helicene with Multiple Redox States. *ChemPlusChem* **2014,** *79* (7), 1030-1035.

19. Ceruti, M.; Balliano, G.; Rocco, F.; Lenhart, A.; Schulz, G. E.; Castelli, F.; Milla, P. Synthesis and biological activity of new iodoacetamide derivatives on mutants of squalene-hopene cyclase. *Lipids* **2005,** *40* (7), 729-35.
20. Kel, O.; Furstenberg, A.; Mehanna, N.; Nicolas, C.; Laleu, B.; Hammarson, M.; Albinsson, B.; Lacour, J.; Vauthey, E. Chiral Selectivity in the Binding of [4]Helicene Derivatives to Double-Stranded DNA. *Chem-Eur J* **2013,** *19* (22), 7173-7180.
21. Kel, O.; Sherin, P.; Mehanna, N.; Laleu, B.; Lacour, J.; Vauthey, E. Excited- state properties of chiral [4]helicene cations. *Photoch Photobio Sci* **2012,** *11* (4), 623-631.
22. (a) Reddy, L. H.; Dubernet, C.; Mouelhi, S. L.; Marque, P. E.; Desmaele, D.; Couvreur, P. A new nanomedicine of gemcitabine displays enhanced anticancer activity in sensitive and resistant leukemia types. *J Control Release* **2007,** *124* (1-2), 20-7; (b) Dosio, F.; Reddy, L. H.; Ferrero, A.; Stella, B.; Cattel, L.; Couvreur, P. Novel nanoassemblies composed of squalenoyl-paclitaxel derivatives: synthesis, characterization, and biological evaluation. *Bioconjugate chemistry* **2010,** *21* (7), 1349-61.
23. Duhem, N.; Danhier, F.; Pourcelle, V.; Schumers, J. M.; Bertrand, O.; Leduff, C. S.; Hoeppener, S.; Schubert, U. S.; Gohy, J. F.; Marchand-Brynaert, J.; Preat, V. Self-assembling doxorubicin-tocopherol succinate prodrug as a new drug delivery system: synthesis, characterization, and in vitro and in vivo anticancer activity. *Bioconjug Chem* **2014,** *25* (1), 72-81.
24. Couvreur, P.; Reddy, L. H.; Mangenot, S.; Poupaert, J. H.; Desmaele, D.; Lepetre-Mouelhi, S.; Pili, B.; Bourgaux, C.; Amenitsch, H.; Ollivon, M. Discovery of new hexagonal supramolecular nanostructures formed by squalenoylation of an anticancer nucleoside analogue. *Small* **2008,** *4* (2), 247-53.
25. Spicer, P. T. Progress in liquid crystalline dispersions: Cubosomes. *Curr Opin Colloid In* **2005,** *10* (5-6), 274-279.
26. Kel, O.; Furstenberg, A.; Mehanna, N.; Nicolas, C.; Laleu, B.; Hammarson, M.; Albinsson, B.; Lacour, J.; Vauthey, E. Chiral selectivity in the binding of [4]helicene derivatives to double-stranded DNA. *Chemistry* **2013,** *19* (22), 7173-80.
27. Wolfbeis, O. S. An overview of nanoparticles commonly used in fluorescent bioimaging. *Chem Soc Rev* **2015,** *44* (14), 4743-4768.
28. Weinberg, S. E.; Chandel, N. S. Targeting mitochondria metabolism for cancer therapy. *Nat Chem Biol* **2015,** *11* (1), 9-15.
29. Yousif, L. F.; Stewart, K. M.; Kelley, S. O. Targeting mitochondria with organelle-specific compounds: strategies and applications. *Chembiochem* **2009,** *10* (12), 1939-50.
30. (a) Dodani, S. C.; Leary, S. C.; Cobine, P. A.; Winge, D. R.; Chang, C. J. A targetable fluorescent sensor reveals that copper-deficient SCO1 and SCO2 patient cells prioritize mitochondrial copper homeostasis. *J Am Chem Soc* **2011,** *133* (22), 8606-16; (b) Dickinson, B. C.; Chang, C. J. A targetable fluorescent probe for imaging hydrogen peroxide in the mitochondria of living cells. *J Am Chem Soc* **2008,** *130* (30), 9638-+; (c) Hu, Q. L.; Gao, M.; Feng, G. X.; Liu, B. Mitochondria-Targeted Cancer Therapy Using a Light-Up Probe with Aggregation-Induced-Emission Characteristics. *Angew Chem Int Edit* **2014,** *53* (51), 14225-14229; (d) Lee, M. H.; Park, N.; Yi, C.; Han, J. H.; Hong, J. H.; Kim, K. P.; Kang, D. H.; Sessler, J. L.; Kang, C.; Kim, J. S. Mitochondria-Immobilized pH-Sensitive Off-On Fluorescent Probe. *J Am Chem Soc* **2014,** *136* (40), 14136-14142.
31. (a) Weinberg, S. E.; Chandel, N. S. Targeting mitochondria metabolism for cancer therapy. *Nat Chem Biol* **2015,** *11* (1), 9-15; (b) Xu, Z.; Xu, L. Fluorescent probes for the

selective detection of chemical species inside mitochondria. *Chem Commun (Camb)* **2016,** *52* (6), 1094-119.
32. Belostotsky, I.; da Silva, S. M.; Paez, M. G.; Indig, G. L. Mitochondrial targeting for photochemotherapy. Can selective tumor cell killing be predicted based on n-octanol/water distribution coefficients? *Biotech Histochem* **2011,** *86* (5), 302-314.
33. Bildstein, L.; Dubernet, C.; Marsaud, V.; Chacun, H.; Nicolas, V.; Gueutin, C.; Sarasin, A.; Benech, H.; Lepetre-Mouelhi, S.; Desmaele, D.; Couvreur, P. Transmembrane diffusion of gemcitabine by a nanoparticulate squalenoyl prodrug: an original drug delivery pathway. *J Control Release* **2010,** *147* (2), 163-70.
34. (a) Bildstein, L.; Marsaud, V.; Chacun, H.; Lepetre-Mouelhi, S.; Desmaele, D.; Couvreur, P.; Dubernet, C. Extracellular-protein-enhanced cellular uptake of squalenoyl gemcitabine from nanoassemblies. *Soft Matter* **2010,** *6* (21), 5570-5580; (b) Sahay, G.; Alakhova, D. Y.; Kabanov, A. V. Endocytosis of nanomedicines. *J Control Release* **2010,** *145* (3), 182-95.
35. Oh, N.; Park, J. H. Endocytosis and exocytosis of nanoparticles in mammalian cells. *Int J Nanomed* **2014,** *9*, 51-63.
36. Wallabregue, A.; Moreau, D.; Sherin, P.; Moneva Lorente, P.; Jarolimova, Z.; Bakker, E.; Vauthey, E.; Gruenberg, J.; Lacour, J. Selective Imaging of Late Endosomes with a pH-Sensitive Diazaoxatriangulene Fluorescent Probe. *J Am Chem Soc* **2016,** *138* (6), 1752-5.
37. Adler, J.; Parmryd, I. Quantifying colocalization by correlation: the Pearson correlation coefficient is superior to the Mander's overlap coefficient. *Cytometry A* **2010,** *77* (8), 733-42.